PHYSICAL REVIEW B VOLUME 16, NUMBER 12 15 DECEMBER 1977

Si (111) 7×7 surface structure: Calculations of LEED intensity and comparison with experiment

J. D. Levine and S. H. McFarlane
RCA Laboratories, Princeton, New Jersey 08540

Peter Mark*
Department of Electrical Engineering, Princeton University, Princeton, New Jersey 08540
(Received 27 June 1977)

Using a Si surface model involving interference between two rippled-surface double layers, a kinematic analysis of low-energy-electron-diffraction (LEED) intensities of all fractional-order spots has been completed and compared with recent experimental LEED 7×7 intensity data. Since the ripple is a small perturbation, the surface is almost ideally terminated; no vacancies or adatoms are required in the model. The intricate 7×7 LEED patterns and their considerable intensity variation with 5-V energy increments are shown to agree with the computed patterns. Threefold rotational symmetry reversals are observed in the LEED patterns at about 20-V intervals and are also computed from the rippled-surface model.

I. INTRODUCTION

It is well known that at a clean, annealed Si(111) surface, the atoms are located in a superlattice whose lateral periodicity is seven times that of the bulk. The low-energy-electron diffraction (LEED) pattern characterizing this surface is called the Si(111) 7×7 pattern; it is perhaps the most repeatable and often discussed LEED pattern in the semiconductor literature.[1-11]

Atomistic models have been proposed to account for the observed 7×7 LEED patterns based on lattice defects (vacancies[1-4] and adatoms[5]) in the terminating lattice plane and on static deformations of the lattice near the surface derived from dynamic instabilities of periodic surface excitations (phonons[12,13] and charge-density waves[14]). No attempts were made in these models to calculate the intensities of the primary and seventh-order LEED beams as a function of primary electron energy. At the present time, experimental Si(111) 7×7 LEED patterns in the literature are given only at selected primary energies and the diffracted beam intensities have not been systematically measured. To document the intensity data in some depth, we have recorded LEED patterns of the Si(111) 7×7 structure at 5-V intervals for primary beam energies in the range 20–340 V. These data and crystal-surface preparations will be described in detail in Sec. IV.

A major finding, evident from examining these newly observed data, is that the fractional-order LEED patterns for $E \gtrsim 70$ V usually have a pronounced 3-fold rotational symmetry. At nearly each 5-V interval, the intensity distribution of the fractional-order LEED pattern changes significantly. At about 20-V intervals, the fractional-order LEED pattern rotational symmetry reverses from +3 fold to −3 fold. In between these ±3-fold symmetries, there is a primary energy where the patterns are nearly 6-fold rotationally symmetric.

The published surface-defect models[1-5] are incapable of yielding fractional order LEED patterns with rotational symmetries that depend on primary electron energy in the single-scattering approximation used here because the surface defects are confined to the terminating lattice plane. This is in direct contradiction to experimental observation.[15,16] To account for the observed rotational-symmetry reversals at 20-V intervals and the significant fractional order LEED pattern intensity variations at 5-V intervals in the single-scattering approximation, a surface deformation such as that developed in Fig. 1 is required. Figure 1(a) depicts four layers (two double layers) of the (111) crystal plane with the surface layer No. 1 being ideally terminated. The lateral direction is $[11\bar{2}]$, which accurately depicts the stacking of Si atoms in the crystal. The nearest-neighbor spacing in the surface region is a_1. Each double layer has a thickness of $\delta_0 = 0.78$ Å, and the double layers repeat every 4×0.78 or 3.12 Å. The diagram shows "dangling bonds" into vacuum caused by the sp^3 hybridization characteristic of the bulk Si crystal. However, it is generally agreed that these dangling bonds of the ideally terminated lattice are unstable, and that the surface atoms relax their positions by contracting inward toward the lattice so as to form a more planar sp^2 type of bond. In Fig. 1(b), these surface atoms are shown relaxed inward by approximately $\frac{1}{2}\delta_0$. From chemical-bonding arguments, Applebaum and Hamann[7] infer that the surface-

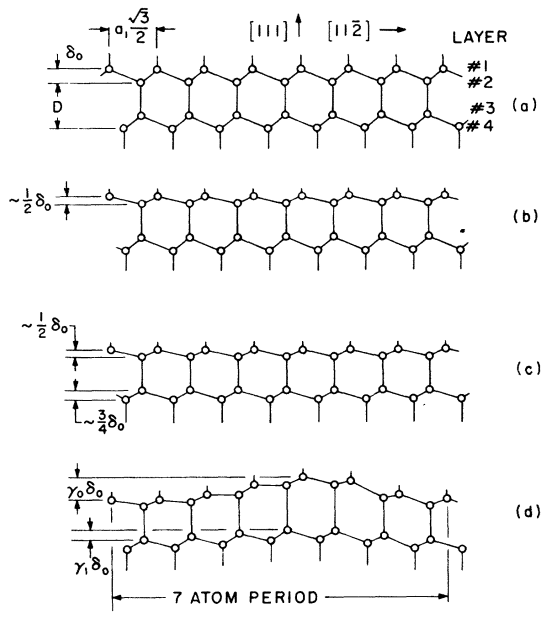

FIG. 1. Schematic of atoms in the Si(111) surface region, and an illustration of how the 7×7 ripple deformation is generated. (a) The ideally terminated lattice with unstable dangling bonds. (b) Relaxation of the surface atoms to form a nearly graphitelike layer. (c) Relaxation of the subsurface atoms. (d) Periodic ripple found by the small amount of residual compressive stress in the surface layers. The ripple amplitudes are shown greatly exaggerated for clarity in (d); in fact, they are treated as a perturbation in the mathematical formalism.

atom relaxation is 0.33 Å; in a later work,[8] they infer from surface-state spectra that the relaxation can be 0.46 Å or greater. Thus, the value of 0.38 Å tentatively chosen here is consistent with their calculations. This change of hybridization from sp^3 to sp^2 is known to introduce a weakening of the π back bonds. Thus the bonding of layer No. 2 to layer No. 3 should be reduced as is the case in graphite compared to diamond. As a consequence, one can anticipate that layer No. 3 will relax inward toward layer No. 4 to form a somewhat more planar double layer with the relaxation of perhaps $\frac{1}{4}\delta_0$, as shown in Fig. 1(c). The magnitude of this type of relaxation decreases with increasing depth into the crystal.

There is excess energy stored in the crystal per unit volume in the surface region because the hybridization in that region is partially sp^2, while the hybridization in the bulk is sp^3. This excess energy per unit volume will produce a uniform hydrostatic pressure. Thus we can anticipate that there may be a residual surface energy and a surface pressure available which can be the driving force for a surface deformation. The usual type of deformation which relaxes the surface energy to some extent is a uniform bowing of the macroscopic crystal into a spherical shell. Another mode of deformation is possible which can relax the surface energy without straining most of the crystal bulk. This mode is a periodic surface ripple which is damped into the bulk, as shown in Fig. 1(d). This periodic deformation is similar in mathematical representation to standing surface waves at fluid interfaces, to electronic surface states, and possibly also to the ripple distortions suggested on the basis of surface phonons and charge-density waves.[12-14] But this is the first time, to the authors' knowledge, that periodic surface ripples have been used as a basis for the direct interpretation of fractional-order LEED beam-intensity variations with primary-electron energy.

In summary, we propose on the basis of experimental analysis of fractional-order LEED beam-intensity variations with primary-electron energy that a ripplelike deformation of at least the top two double atomic layers is responsible for the 7×7 superlattice of the annealed Si(111) surface. It is not clear at this writing whether periodic stress relaxation of rehybridization energy or periodic static deformation owing to dynamic instabilities of periodic surface excitations, are responsible for the ripple deformation nor is it clear that these various phenomena are distinct. It is clear that surface-layer atomic defect models by themselves cannot account for the experimental observations although they may coexist with the ripple distortions. We will not speculate further on the origin of the 7×7 periodicity. Rather, as in all the existing atomic surface models,[1-14] we will accept this superlattice as an experimental fact. Our unique contribution is to use a ripple model to calculate the fractional-order LEED beam intensities from single-scattering theory and to compare these calculated intensities with experimental LEED intensity data. For the Si(111) 7×7 surface, symmetry requires that the 7-fold surface ripple have triangular lateral periodicity, as shown in Fig. 2. Each side of each triangle has seven atoms. The dashed line is the [11$\bar{2}$] direction in the surface plane, along which the elevation in Fig. 1 was drawn. The shading is a measure of the surface-atom height in the ripple deformation, that is, a measure of the ripple amplitude.

The paper is arranged as follows. Sec. II is devoted to the theoretical formulation of the ripple model. Experimental data will be introduced to narrow the theoretical options. The fractional-order LEED intensities are calculated in

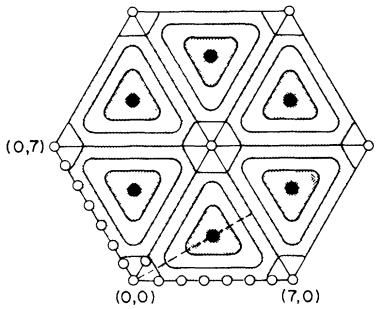

FIG. 2. Schematic of atomic-height deformation $Z(s,t)$ in the Si(111) 7×7 surface plane. The magnitude of deformation is proportional to the shading. The dashed line indicates the $[11\bar{2}]$ direction along which Fig. 1 was constructed.

Sec. III, and in Sec. IV, the computed and experimental LEED patterns are compared. The conclusions are discussed in Sec. V.

II. THEORY

The objective of the new model is to reproduce the rotational symmetry variations with primary beam energy of the experimental fractional-order LEED patterns. It is not our intention to present a detailed multiple-scattering computation of the beam-intensity primary-energy dependence of every fractional-order beam. In fact, the latter undertaking would be impossible. A complete dynamical scattering analysis of the proposed surface structure is out of the question with presently available computer capabilities. There are far too many atoms in the unit cell. Therefore, following the procedures established by Duke and Tucker,[17] it suffices to compute the kinematical (single scattering) Bragg envelopes of the normal incidence, fractional-order beam intensity profiles in order to analyze the rotational symmetry variation with primary-beam energy of the fractional-order beams.

The lattice scattering factor in this kinematical formulation is given by

$$f=\sum_{n=1}^{\infty}\sum_{\vec{r}_n}^{49}\exp[i(\vec{k}_{\parallel}\cdot\vec{r}_n)]\exp\{i[k'_{\perp}Z_n(\vec{r}_n)]\}. \tag{1}$$

This is a sum over all the atoms in the n layers comprising the lattice. The nth layer has 49 atoms in the unit cell; each of these atoms has a lateral coordinate $\vec{r}_n$ and a depth coordinate $Z_n(\vec{r}_n)$. Because of the proposed ripple deformation, $Z_n(\vec{r}_n)$ is a 7-fold periodic function of the lateral coordinate $\vec{r}_n$. In Eq. (1), the lateral wave vector is $\vec{k}_{\parallel}$ and the normal wave vector is $k_{\perp}=2\pi/\lambda$. Here $\lambda=[150/(V+10)]^{1/2}$ (λ is in angstroms, V in volts), V is the experimentally measured voltage of the scattered electron beam in vacuum, and 10 V is a reasonable value of the inner potential for Si. Because the incident beam is at normal incidence and the exit beam is at angle θ, $k_{\perp}$ is multiplied by $(1+\cos\theta)$, to yield

$$k'_{\perp}=2\pi(V+10)^{1/2}150^{-1/2}(1+\cos\theta), \tag{2}$$

as required in Eq. (1).

It is convenient to consider $Z_n(\vec{r}_n)$ as the sum of one component which is independent of the ripple and another component which depends only on the ripple,

$$Z_n(\vec{r}_n)=\zeta_n+\gamma_n\delta_0F(\vec{r}_n). \tag{3}$$

Here ζ_n is the ripple-independent part; for an ideally terminated lattice with $n=1, 2, 3, \ldots$, it can be seen from Fig. 1(a) that $\zeta_n=0$, $\frac{1}{4}D$, D, $1\frac{1}{4}D$, $2D$, $2\frac{1}{4}D$, ..., where D is the double-layer periodicity given in terms of the lattice constant a_0 by $D=a_0/\sqrt{3}=3.12$ Å. The double layer thickness is $\delta_0=\frac{1}{4}D$. Each layer is assumed to have its own ripple amplitude $\gamma_n\delta_0$ and a common ripple shape factor $F(\vec{r}_n)$ as in similar problems of surface waves on liquids or surface electronic states. The combination of Eqs. (1) and (2) yields

$$f=\sum_{n=1}^{\infty}\exp[i(k'_{\perp}\zeta_n)]\sum_{\vec{r}_n}^{49}\exp[i(\vec{k}_{\parallel}\cdot\vec{r}_n)]\times\exp\{i(\vec{k}'_{\perp}\gamma_n\delta_0F(\vec{r}_n)\}. \tag{4}$$

Since the ripple amplitude $\gamma_n\delta_0$ is small for all layers, it is considered a perturbation and the exponential on the far right-hand side in Eq. (4) can be expanded to yield

$$f=\sum_{n=1}^{\infty}\exp[i(k'_{\perp}\zeta_n)]\sum_{\vec{r}_n}^{49}\exp[i(\vec{k}_{\parallel}\cdot\vec{r}_n)]\times[1+ik'_{\perp}\gamma_n\delta_0F(\vec{r}_n)]. \tag{5}$$

It can be shown for the Si(111) 7×7 lattice that

$$\vec{k}_{\parallel}\cdot\vec{r}_n=\tfrac{1}{7}2\pi(ls_n+mt_n), \tag{6}$$

where l and m are integers describing the lateral wave vector and $\vec{k}_{\parallel}=l\hat{l}+m\hat{m}$, where $\frac{1}{7}2\pi\hat{l}$ and $\frac{1}{7}2\pi\hat{m}$ are the unit wave vectors at 60° to each other. Also, s_n and t_n are integers and multiples of $\frac{1}{3}$ describing the lateral location of each atom referred to the surface plane and $\vec{r}_n=s_n\hat{s}+t_n\hat{t}$, where $\hat{s}$ and $\hat{t}$ are the unit spatial vectors at 120° to each other. The nearest-neighbor distance in the first layer is $a_1=|\hat{s}|=a_0/\sqrt{2}=3.831$ Å.

Fractional-order LEED beams are defined as those for which l and m are all integers except for multiples of seven. For fractional-order beams it follows from symmetry that $\sum_r\exp[i(\vec{k}_{\parallel}\cdot\vec{r})]=0$. A well-known example of this

in one dimension is

$$\sum_{n=0}^{N-1} \exp\left(2\pi i n \frac{l}{7}\right) = 0 ,$$

which holds for all values of the integer l except for multiples of seven. Only the fractional-order beams are of interest here as the deformation gives rise to the fractional-order beams, while the undeformed lattice produces the integral-order beams (i.e., l and m multiples of seven). Hence, the lattice scattering factor for an individual *fractional-order* beam is obtained from Eq. (5) by retaining only the second term of the last square bracket,

$$f = ik_1'\delta_0 \sum_{n=0}^{\infty} \gamma_n \exp[i(k_1'\zeta_n)] \sum_{\vec{r}_n}^{49} F(\vec{r}_n) \exp[i(\vec{k}_{\parallel} \cdot \vec{r}_n)] . \tag{7}$$

There are too many unknowns (γ_n, ζ_n) for each n to proceed further without obtaining assistance from experimental LEED data. Let us then consider the magnitude of the phase shift $\psi_{nm} = k_1'(\zeta_n - \zeta_m)$ between layers for various primary energies. Consider first the phase shift between the first and third layers of the ideal periodicity D: $\psi_{13} = 2\pi(1+\cos\theta)(V/150)^{1/2}D$. For an average experimental value of $\cos\theta = 0.88$, this yields $\psi_{13} = 3.01\sqrt{V}$. Consider how ψ_{13} varies in a 5-V interval near 100 V

$$\psi_{13}(105) - \psi_{13}(100) = 3.01(\sqrt{105} - \sqrt{100}) = 0.74 \text{ rad} . \tag{8}$$

Thus, this term accounts for an appreciable fraction of a radian (42.4°) in phase shift for only a 5-V primary-energy interval. It is expected that a LEED pattern would be different with such an appreciable phase change since sin42.6° and cos42.6° are considerably different from their unperturbed values 0 and 1, respectively. The data to be described in more detail later shows that 5-V primary-energy increments significantly changes the fractional-order LEED pattern near 100 V. We conclude that this 5-V experimentally observed variation can be accounted for by interference between at least two layers of separation D. This is the spacing between double layers.

Next, consider the phase shift ψ_{12} between the first two layers which constitute the first double layer. It has already been suggested that the driving force for the ripple deformation is the change of hybridization from sp^3 to sp^2 in the surface double layer. Thus, the spacing of the first double layer relaxes perhaps to $\frac{1}{2}\delta_0$ or $\frac{1}{8}D$. Using the same arguments given above, it follows that this phase shift energy dependence near 100 V is

$$\psi_{12}(105) - \psi_{12}(100) = 0.38(\sqrt{105} - \sqrt{100}) = 0.093 \text{ rad} = 5.3^\circ . \tag{9}$$

This shift is too small to account for an appreciable fractional-order LEED pattern change in 5-V intervals, since $\sin 5.3^\circ \sim 0$ and $\cos 5.3^\circ \sim 1$. We conclude that in comparing Eqs. (8) and (9) with LEED data, the most important terms to retain are those which give scatterings *between* double layers and we choose to neglect, for a first approximation, the terms which give scattering *within* a double layer. In particular, we will consider only the first two double layers in this problem, i.e., $\gamma_5, \gamma_6, \gamma_7, \gamma_8, \ldots = 0$. Furthermore, we will consider the double layers to be so close together *compared to* D that each double layer will be approximated mathematically by a planar layer, i.e., $\zeta_1 = \zeta_2$, $\zeta_3 = \zeta_4$, $\gamma_1 = \gamma_2$, and $\gamma_3 = \gamma_4$. Each planar layer therefore has a nearly graphitelike Si structure, which is known for at least one crystal in nature[18]: β-USi_2. We use these simplifications because they highlight the main features of the data, without introducing what we consider to be unnecessary and unmanagable mathematical complications.

The consequence of the above simplifications is that Eq. (7) can be written as

$$f = ik_1'\delta_0\gamma_1 \sum_{\vec{r}}^{98} F(r) \exp[i(\vec{k}_{\parallel} \cdot \vec{r})] + ik_1'\delta_0\gamma_3 \exp[i(k_1'D)] \sum_{\vec{r}}^{98} F(r') \exp[i(\vec{k}_{\parallel} \cdot \vec{r}')] , \tag{10}$$

where, for simplicity in notation, $\vec{r}$ and $\vec{r}'$ are introduced to indicate each of the atom locations in the first and second graphitelike *double* layers, respectively. There are $2 \times 49 = 98$ atoms in each double layer 7×7 unit cell. The relationship of $\vec{r}'$ to $\vec{r}$ is needed to combine the terms in Eq. (10). For every atom location $\vec{r}'$, in one graphitelike plane there are three translational vectors $\vec{\tau}_1, \vec{\tau}_2, \vec{\tau}_3$ between the three nearest-neighbor atom locations $\vec{r}_1$, $\vec{r}_2$, and $\vec{r}_3$ in the other graphitelike plane, as shown schematically in Fig. 3(a). These translational vectors referred to the unit vector $\hat{s}$ and $\hat{t}$, are

$$\vec{\tau}_1 = (\tfrac{2}{3}, \tfrac{1}{3}); \quad \vec{\tau}_2 = (-\tfrac{1}{3}, \tfrac{1}{3}); \quad \vec{\tau}_3 = (-\tfrac{1}{3}, -\tfrac{2}{3}) \tag{11}$$

and are easily derived from inspection of Fig. 3(b). It is also evident from Fig. 3(a) that $\vec{r}'$ can be represented in three equivalent ways

$$\vec{r}' = \vec{r}_1 + \vec{\tau}_1; \quad \vec{r}' = \vec{r}_2 + \vec{\tau}_2; \quad \vec{r}' = \vec{r}_3 + \vec{\tau}_3 . \tag{12}$$

The two graphitelike layers are offset from each other by either of the three equivalent vectors $\vec{\tau}_1, \vec{\tau}_2, \vec{\tau}_3$. By summing Eq. (12) it can be shown that

$$\vec{r}' = \frac{1}{3}\sum_{\mu=1}^{3}\vec{r}_\mu , \tag{13}$$

since $\vec{\tau}_1+\vec{\tau}_2+\vec{\tau}_3=0$. Thus $\vec{r}'$ is given as the average of the lateral distances in three nearest neighbors in the other plane. By analogy we assert that the shape factor in the second graphitelike layer is also the arithmetic average of the three nearest neighbors in the first graphitelike layer

$$F(\vec{r}')=\frac{1}{3}\sum_{\mu=1}^{3}F(\vec{r}_\mu) . \tag{14}$$

This assertion incorporates the appropriate 3-fold rotational symmetry evident from inspection of the two graphitelike layer stacking as shown in Fig. 4 and from the following argument. These layers are offset laterally by either $\vec{\tau}_1$, $\vec{\tau}_2$, or $\vec{\tau}_3$ which are equivalent by symmetry for flat layers. But in the presence of a rippled superlattice, the depth dimension is a function of the $\vec{\tau}$'s, so the $\vec{\tau}$'s are no longer equivalent. One alternative possible shape factor, given by $F_1(\vec{r}')=F(\vec{r}_1+\vec{\tau}_1)$ would yield a computed LEED pattern with a pronounced reflection symmetry, because $\vec{\tau}_1$ is preferred over $\vec{\tau}_2$ and $\vec{\tau}_3$. Still another possible shape factor,

$$F_2(\vec{r}')=\frac{1}{6}\sum_{\mu=1}^{3}F(\vec{r}_\mu)+F(-\vec{r}_\mu) ,$$

would yield computed LEED patterns with perfect 6-fold symmetry. These reflection and 6-fold symmetries are contrary to experimental LEED data.

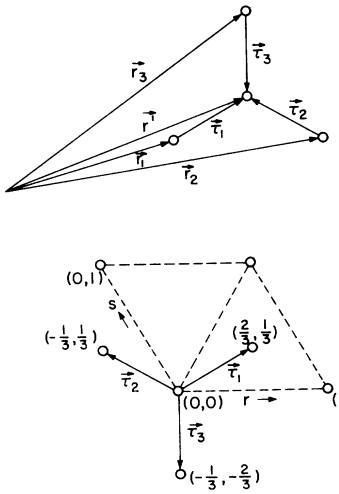

FIG. 3. Relationship between a surface vector $\vec{r}$ and a subsurface vector $\vec{r}'$ in the graphitelike layers. (a) Vector diagram. (b) Detail showing definition of unit translational vectors $\vec{\tau}_m$ which offset the surface and subsurface graphitelike layers.

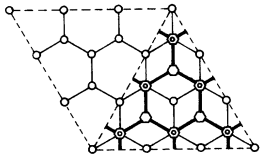

FIG. 4. Overlay showing how the two graphitelike layers are offset by either $\vec{\tau}_1$, $\vec{\tau}_2$, or $\vec{\tau}_3$. The subsurface layer is shown as that portion with hexagonal shapes for atom locations and thicker lines joining the atoms.

The selected shape factor given in Eq. (14) is the only one of the above choices which incorporates the threefold symmetry needed to reproduce the observed LEED data.

By combining Eq. (14) with Eq. (10), we obtain

$$f = ik_\perp'\delta_0\gamma_1\sum_{\vec{r}}^{98}F(\vec{r})\exp[i(\vec{k}_\parallel\cdot\vec{r})]$$
$$+\tfrac{1}{3}ik_\perp'\delta_0\gamma_3\exp[i(k_\perp'D)]$$
$$\times\sum_{\mu=1}^{3}\sum_{\vec{r}_\mu}^{98}F(\vec{r}_\mu)\exp[i(\vec{k}_\parallel\cdot\vec{r}')] . \tag{15}$$

But from Eq. (12) we have $\vec{r}'=\vec{r}_\mu+\vec{\tau}_\mu$, for all μ. When this relation is substituted for $\vec{r}'$ in the last term of Eq. (15), that term becomes

$$\sum_{\mu=1}^{3}\sum_{\vec{r}_\mu}^{98}F(\vec{r}_\mu)\exp[i(\vec{k}_\parallel\cdot\vec{r}')]$$
$$=\sum_{\mu=1}^{3}\sum_{\vec{r}_\mu}^{98}F(\vec{r}_\mu)\exp\{i[\vec{k}_\parallel\cdot(\vec{r}_\mu+\vec{\tau}_\mu)]\}$$
$$=\sum_{\mu=1}^{3}\exp[i(\vec{k}_\parallel\cdot\vec{\tau}_\mu)]\sum_{\vec{r}_\mu}^{98}F(\vec{r}_\mu)\exp[i(\vec{k}_\parallel\cdot\vec{r}_\mu)]$$
$$=\sum_{\mu=1}^{3}\exp[i(\vec{k}_\parallel\cdot\vec{\tau}_\mu)]\sum_{\vec{r}}^{98}F(\vec{r})\exp[i(\vec{k}_\parallel\cdot\vec{r})] . \tag{16}$$

The final form of Eq. (16) follows by symmetry, since in a sum over all 98 atoms in the 6-fold rotationally symmetric graphitelike superlattice, it makes no difference whether the origin of coordinates is chosen to be at $\vec{\tau}_1$, $\vec{\tau}_2$, or $\vec{\tau}_3$. By combining Eqs. (15) and (16) and grouping of terms we finally obtain

$$f = ik_\perp'\delta_0\gamma_1\left(1+\gamma\exp[i(k_\perp'D)]\sum_{\mu=1}^{3}\exp[i(\vec{k}_\parallel\cdot\vec{\tau}_\mu)]\right)$$
$$\times\sum_{\vec{r}}^{98}F(\vec{r})\exp[i(\vec{k}_\parallel\cdot\vec{r})] , \tag{17}$$

where

$$\gamma = (\tfrac{1}{3})(\gamma_3/\gamma_1),$$
$$\vec{k}_{\parallel}\cdot\vec{\tau}_1 = (2\pi/7)(2l/3+m/3),$$
$$\vec{k}_{\parallel}\cdot\vec{\tau}_2 = (2\pi/7)(-l/3+m/3),$$
$$\vec{k}_{\parallel}\cdot\vec{\tau}_3 = (2\pi/7)(-l/3-2m/3).$$

It can be shown that $\cos\theta$ needed in the leading $k'_\perp$ term [see Eq. (2)] is given by

$$\cos\theta = (1-\vec{k}_{\parallel}\cdot\vec{k}_{\parallel}/k_1^2)^{1/2} \tag{18}$$

for the Si(111) 7×7 surface, where

$$\vec{k}_{\parallel}\cdot\vec{k}_{\parallel} = [(l+m\cos60^\circ)^2+(m\sin60^\circ)^2] \times[(2\pi/7a_1)\cos30^\circ]^2. \tag{19}$$

III. CALCULATION OF LEED INTENSITY

It is convenient to write Eq. (17) in a shorthand notation as

$$f = ik_\perp\delta_0\gamma_1 R(\theta)T(l,m,\gamma,V)G(l,m), \tag{20}$$

where $R(\theta)=1+\cos\theta$; $T(l,m,\gamma,V)=1+\gamma\exp[i(k'_\perp D)] \times\sum_{\mu=1}^{3}\exp[i(\vec{k}_{\parallel}\cdot\vec{\tau}_\mu)]$; $G(l,m)=\sum_{\vec{r}}^{98}F(\vec{r})\exp[i(\vec{k}_{\parallel}\cdot\vec{r})]$. The $R(\theta)$ term depends only on θ; it is chosen to cut off abruptly at $\theta=40^\circ$, because the LEED display screen used in the data collection subtends that half angle. The $G(l,m)$ term is 6-fold symmetric and repeats every third unit cell in reciprocal space. The term of most interest for comparison with experimental LEED data is the translational term $T(l,m,\gamma,V)$. This is 3-fold symmetric, depends on primary energy, and also repeats every third unit cell in reciprocal space. This is the term most responsible for the intricate fractional-order LEED patterns and their variations with primary-beam energy.

The LEED intensities I are given by $|f|^2$,

$$I(l,m,\gamma,V) = (k\delta_0\gamma_1)^2R^2(\theta)\,|T(l,m,\gamma,V)|^2G^2(l,m), \tag{21}$$

and $|T(l,m,\gamma,V)|^2$ can be explicitly written as

$$|T(l,m,\gamma,V)|^2 = 1+2\gamma(\cos\phi_1+\cos\phi_2+\cos\phi_3) +\gamma^2\{3+2[\cos(\phi_1-\phi_2)+\cos(\phi_2-\phi_1) +\cos(\phi_3-\phi_1)]\}, \tag{22}$$

where

$$\phi_\mu = k'_\perp D+\vec{k}\cdot\vec{\tau}_\mu, \quad \mu=1,\,2,\,3. \tag{23}$$

For analysis of 3-fold rotational symmetry reversals, it is more convenient to write $T(l,m,\gamma,V)$ in phasor form,

$$T(l,m,\gamma,V) = 1+\gamma\exp(ik'_\perp D)\exp(i\beta+\epsilon), \tag{24}$$

where β and ϵ are real functions of l and m. It also follows that in a 3-fold rotational symmetry reversal where $l\to-l, m\to-m$, there is a phase reversal $\beta\to-\beta$, so that

$$T(-l,-m,\gamma,V) = 1+\gamma\exp(ik'_\perp D)\exp(-i\beta+\epsilon). \tag{25}$$

The absolute values of these terms are

$$|T(l,m,\gamma,V)|^2 = 1+\gamma^2\exp(2\epsilon) +2\gamma\exp[\epsilon\cos(k'_\perp D+\beta)] \tag{26a}$$

$$|T(-l,-m,\gamma,V)|^2 = 1+\gamma^2\exp(2\epsilon) +2\gamma\exp[\epsilon\cos(k'_\perp D-\beta)]. \tag{26b}$$

The condition when $|T(l,m,\gamma,V)|^2 = |T(-l,-m,\gamma,V)|^2$ is special; it signifies that there is a perfect 6-fold rotational symmetry. This 6-fold condition is given by

$$\cos(k'_\perp D+\beta) = \cos(k'_\perp D-\beta), \tag{27}$$

and occurs for all values of β (all beams l,m) whenever

$$k'_\perp D = N\pi, \quad N=\text{integer}. \tag{28}$$

Substituting the definition for $k'_\perp$ from Eq. (2) into the above, we can solve for the primary-beam voltage V_6 corresponding to 6-fold rotational symmetry,

$$V_6 = 150[N/2D(1+\cos\theta)]^2-10. \tag{29a}$$

It is important to emphasize that the above symmetry arguments are completely independent of the values of γ or $G(l,m)$. The average value of θ between the maximum 45° and minimum 10° used in collecting the data is $\bar{\theta}=27.5^\circ$. Using $\cos\bar{\theta}=0.887$, and $D=3.12$ Å in the above, we have

$$V_6 = 1.081N^2-10, \tag{29b}$$

which will be compared with experimental data in Sec. IV.

The $G(l,m)$ function was not computed from first principles, since $F(\vec{r})$ is unknown at this stage. Rather a simplified form of $G(l,m)$ was selected which fits the data presented in Sec. IV. Since the term $G(l,m)$ is 6-fold symmetric, it will merely increase the line intensity connecting the primary spots in the LEED patterns. We have chosen a functional form

$$G(l,m) = C+\epsilon_l+\epsilon_m+\epsilon_{l+m}, \tag{30}$$

where C is a constant and the other terms are given by

$$\epsilon_x = \begin{cases} 1 & \text{for } x, \text{ a multiple of 7} \\ 0 & \text{otherwise}, \end{cases} \tag{31}$$

with $x=l$, m or $l+m$. Therefore, for a fractional-order LEED beam on any coordinate line $(l,0)$, $(0,m)$, or $(l,-m)$ we have $G^2(\text{line})=(C+1)^2$, while

for the fractional order beams off a coordinate line, $G^2(\text{no line}) = C^2$. Thus, the ratio of intensities of coordinate lines in the LEED pattern to the rest of the LEED pattern is determined by the parameter C. We chose $C = 3$ for the comparison of computation and experiment given in Sec. IV. It should be stressed again that $G(l, m)$ is independent of V; it contributes nothing significant to the 3-fold intricacies of the LEED pattern. This implies that $F(\vec{r})$ is not a critical function for the comparison of computation and experiment in accounting for LEED pattern rotational symmetry variations. However, a specific selection of $F(\vec{r})$ will determine the distribution of intensity among the fractional-order beams. For example, in the limit $F(\vec{r}) \equiv 0$ (i.e., a perfectly unrippled layer) all fractional order beam intensities vanish, as seen, for example, from Eq. (7).

IV. COMPARISON OF LEED THEORY AND EXPERIMENT

In this section we review how the experimental data was obtained, show and tabulate the data, describe how the theoretical Eq. (21) was analyzed by computer to display computed fractional-order LEED patterns, and finally compare computed and experimental data in some detail.

The LEED patterns were obtained from a four-grid Varian 120 display-type LEED-AES (Auger electron spectroscopy) system with a rotatable, temperature controlled sample manipulator. The half angle of the LEED optics was 40°. The suppressor grid of the LEED optics filtered out the inelastically scattered electrons that suffered an energy loss greater than about 10 V. The LEED intensities were recorded photographically at room temperature at a base pressure of 5×10^{-10} Torr (6.8×10^{-8} Pa). The silicon sample was a (111) oriented single crystal (n type, $n \simeq 10^{16}$ cm^{-3}) whose surface was prepared by chemical polishing. The surface was ordered in the vacuum system by resistive heating using tantalum tape electrodes. The crystal dimensions were: area—

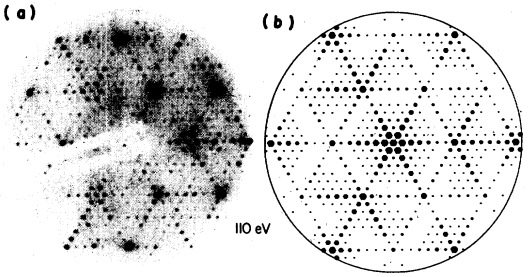

FIG. 6. "Star" LEED pattern at 110 V; (a) experimental, (b) theoretical.

1.27×0.64 cm; thickness—0.16 cm. The (7×7) reconstruction pattern was obtained directly by heating the sample to 1200 °C (measured with an optical pyrometer) for about 15 sec, switching off the heater current and allowing the sample to cool to room temperature. AES was used to determine the cleanliness of the surface. Measurements with an axially integral gun 3 kV cylindrical mirror analyzer revealed only silicon structure in the AES spectrum.

The LEED patterns were recorded photographically from the display screen on 35 mm Kodak Tri-X (ASA 400) film. Photographs were recorded at 5-V intervals and no photographic run took longer than one-half hour. After that time interval, an AES spectrum was again taken to check surface cleanliness. No contaminant from the residual gases in the vacuum chamber were observed after this half-hour interval. Nevertheless, after each photographic run the sample was reannealed as described above. Typical primary-electron beam currents for recording the LEED patterns were in the low microamp range. Precautions were taken to shield out stray magnetic fields which might distort the LEED pattern symmetry.

Examples of LEED patterns observed experimentally and computed theoretically are shown in Figs. 5–9 for primary-beam voltages V in 5-V intervals over the range 105–125 V. Panel (a) of

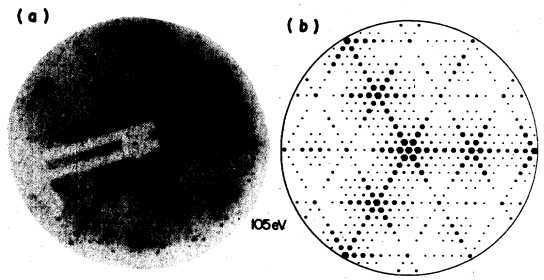

FIG. 5. "Thin propeller" LEED pattern at 105 V; (a) experimental, (b) theoretical.

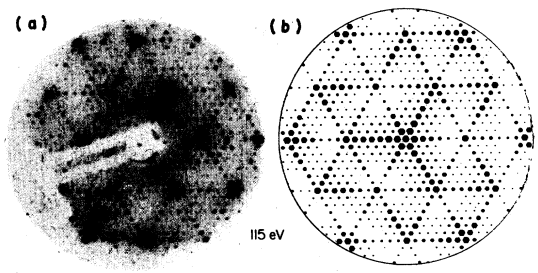

FIG. 7. Modified "star" LEED pattern at 115 V; (a) experimental, (b) theoretical.

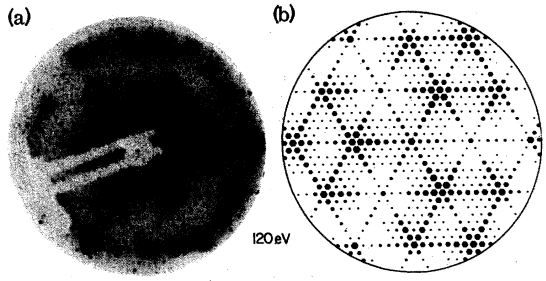

FIG. 8. "Ballantine three ring" LEED pattern at 120 V. (a) experimental. (b) theoretical.

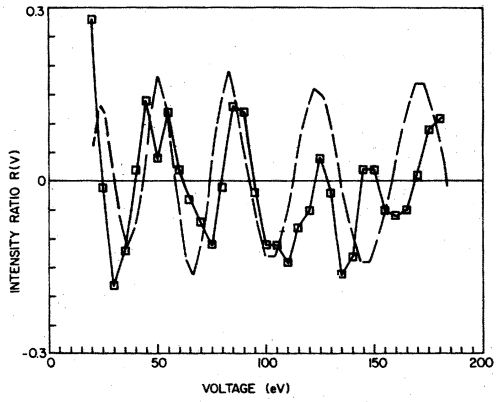

FIG. 10. Plot showing symmetry reversal as a function of voltage. The symmetry ratio $R(V)$ is calculated from Eq. (32), and is an objective measure of the symmetry in the LEED pattern. Patterns with voltages at $R=1$ are six-fold symmetric; those with $R>1$ and $R<1$ have (+) and (−) pattern symmetries, respectively. The squares are experimental; the dashed curve is theoretical.

Fig. 5 is an experimental LEED pattern (negative print for clarity) at 105 V and panel (b) is the corresponding computed LEED pattern at the same experimentally determined voltage (105 V) of the electrons in vacuum. It is worth repeating here that a 10-V constant inner potential has already been included in the theoretical analysis, starting with Eq. (2). That is, the scattering voltage inside the crystal has been taken as 115 V in the example of Fig. 5. Similar comparisons of experiment and computation are given in Figs. 6–9. These experimental and computed LEED patterns show a striking progression of rotational symmetry from a "thin propeller" at 105 V, to a "star" at 110 V, to a "modified star" at 115 V, to a "Ballantine three ring" at 120 V, to a "modified triple ring" at 125 V. The 3-fold rotational symmetries at 105 and 125 V are clearly reversed.

All computed LEED patterns were generated with the following inputs. Equation (21) was solved by computer. The parameter γ was given the value $\gamma=-0.1$ through best fit (subjective) to the data, although fairly good fits were also obtainable using $\gamma=+0.1$. The parameter C in Eq. (30) was given the value 3 in order to give a good ratio of spot intensities along the symmetry lines $(l,0)$, $(0,m)$, compared to the other spot intensities.

It is worth repeating here that the intensities of the computed *integral-order beams* are not tobe compared with corresponding experimental beams since most contributions to the intensities of these beams have been excluded by symmetry in Eq. (7).

The computed pattern intensities were normalized according to the following rule. After the intensities were computed for all beams according to Eq. (21), the fractional-order beams with maximum and minimum intensities were found by a search routine. The intensities were normalized by setting the minimum intensity at zero and the maximum intensity at unity. A graphic display was generated which prints out a hexagonal "spot" of the proper size to scale with the intensity of the beam. The computed LEED patterns of Figs. 5(b)–9(b) were obtained from this display.

An experimental determination of the rotational symmetry reversals was obtained from the fol-

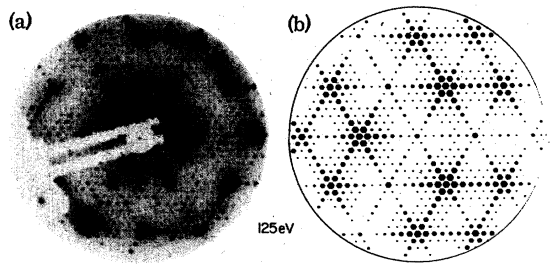

FIG. 9. Modified "Ballantine three ring" LEED pattern at 125 V. (a) experimental. (b) theoretical.

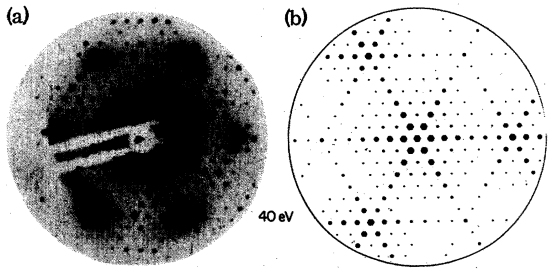

FIG. 11. Typical very low voltage (40 V) LEED patterns, showing nearly 6-fold symmetry and voltage dependence in the experimental pattern (a) but not in the theoretical pattern (b). Because the electron mean-free path is very small, only one graphitelike layer primarily contributes to the scattering.

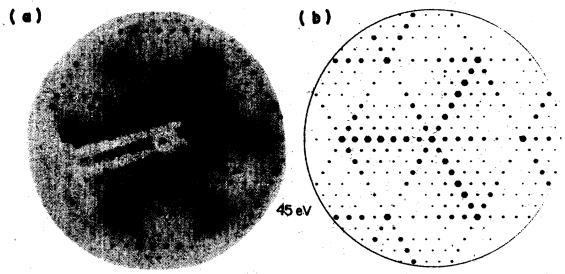

FIG. 12. Same as in Fig. 11, with $V = 45$ V.

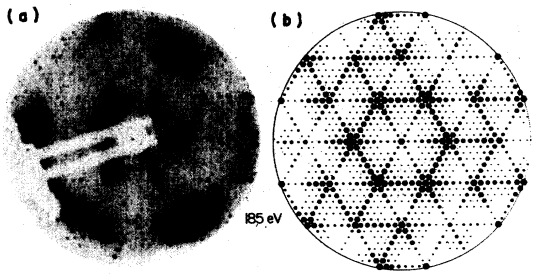

FIG. 14. Same as in Fig. 12, except $V = 185$ V.

lowing objective procedure. A symmetry ratio function $R(V)$ was calculated at each voltage according to the following formula

$$R(V) = \frac{\sum_l' I(l, 0, V) - \sum_l' I(-l, 0, V)}{\sum_l' I(l, 0, V) + \sum_l' I(-l, 0, V)} . \qquad (32)$$

The sums are over all *fractional-order* beams (indicated by primes) in the line from near the center to the edge of the pattern. This ratio is plotted as squares in Fig. 10 as a function of primary energy over the range 20–200 V. It seems that $R(V)$ has a nearly sinusoidal variation, with a period of ~20 V near 100 V.

A periodic variation is expected according to the symmetry reversal arguments described earlier. Indeed by differentiating the theoretical Eq. (29b) the symmetry reversal occurs at $dV_6/dN = 2.162N$, which near $V_6 = 100$ V becomes a 22-V interval. This is the same as the experimental interval in that range. For a more complete test between computation and experiment, the $R(V)$ function in Eq. (32) was computed beam by beam using Eq. (21). As before, the integral-order beams were ignored. The $R(V)$ function computed this way is shown in Fig. 10 by the dashed curve. It also shows a nearly sinusoidal variation as expected from the experimental data and anticipated from the theoretical symmetry reversal argument above. Agreement is good in the range of ~50–130 V.

For silicon, the mean free path of electrons in the lattice is $\simeq 0.7\sqrt{V}$ Å, provided $V \gtrsim 10$ V. Thus, at 40 V or less the mean-free path is much smaller than that at 100 V. As a consequence, we expect that at 20–40 V the beam penetrates primarily only one of the graphitelike layers described above in Sec. II. Thus, for these low-primary energies, the LEED pattern intensities should be nearly 6-fold symmetric, energy independent, and should not agree with theory based on two graphitelike layers. These predictions are in agreement with experimental data, as seen in the typical LEED patterns of Figs. 11(a), taken at 40 V, and 12(a), taken at 45 V. As expected from the above argument, the computed patterns in Figs. 11(b) and 12(b) *do not* agree with the data in this low-voltage range. On the other hand, for voltages higher than 150 V, the primary beam could penetrate perhaps three graphitelike double layers, instead of the two assumed in Eq. (20). As a result, the patterns for $V \gtrsim 150$ V should show new effects due to interferences between three graphitelike layers. This is observed experimentally. At 180 V, a light disk is present in the central section of the LEED pattern as shown in Fig. 13(a). At 185 V, this light disk expands somewhat as shown in Fig. 14(a). The light disk pattern does not agree with theory in Figs. 13(b) and 14(b); in fact, the light disk is not obtainable from Eq. (21), given any combination of γ or C.

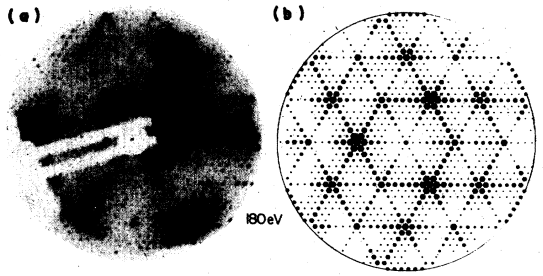

FIG. 13. Typical very-high-voltage LEED pattern. Notice the disk of low-spot intensity. Because the mean free path is large, perhaps three graphitelike layers contribute to the scattering pattern, which cannot be accounted for with only two graphitelike layers in the model. $V = 180$ V. (a) experimental. (b) theoretical.

V. DISCUSSION

While other models[1-14] have been proposed for the 7×7 pattern on Si(111), none have incorporated the symmetries and energy dependences obtainable from the experimental LEED patterns.

It is the thrust in this work to first examine the energy dependence and rotational symmetry behavior of the experimental fractional-order LEED patterns, and then to use this information to eliminate many possible atomic surface structure models. In this manner, the models of Lander and Morrison,[1] and Phillips[2,3] comprising 13 Si-atom vacancies in the topmost layer unit cell are ruled out. The model of Harrison[5] involving 13 Si adatoms instead of vacancies arranged in the same manner also is similarly ruled out. Haneman's model[4] involves rumpled 2×1 layers with raised (R) and lowered (L) atoms which are arranged with stacking faults in a 7-fold fashion such as $|LRLRLRL|LRLRLRL|$, etc. It was not speculated why these peculiar sequences occur, or how the 2×1 rumpled layers intersect in three directions. Nevertheless, it is the only one of the above models which conceivably could yield some energy dependence in a one-dimensional version of the LEED pattern, although it is far too weak to account for the 5-V variations observed in the data.

It is also evident in all the existing defect models[1-3,5] that a subperiod of two-atom units is preferred over others, except for the seven-atom period constituting the superlattice. Thus, a LEED pattern derived from a model with this preferred 2-fold subperiod might have extra fractional-order beams comprising a 2×2 reconstruction. These extra half-integral order beams are *not* observed in the voltage range from 20 V to at least 235 V.

The periodic stress relaxation ripple model suggested here incorporates scattering from 196 perturbed atoms and accounts for the observed 5-V primary energy variations in the fractional order-LEED patterns, for the periodic rotational symmetry reversals, as seen in Fig. 10, and for certain details in the LEED patterns, as seen in Figs. 5–9. The model generates no *additional* (e.g., 2-fold) subperiods; only the pure 7-fold subperiod evident in the experimental data.

Finally, the symmetry arguments described above are very general and are not dependent on the selection of values for the fitting parameters γ and C, which are chosen merely for best fits to the LEED pattern details. At extremely low and high voltages new effects appear, as expected, in the LEED patterns. These are caused by the variation of the electron mean free path with primary energy and associated change in the number of lattice layers participating in the scattering.

The stress relaxation ripple model has a driving force which in our model originates from the change of bond hybridization from pure sp^3 to more sp^2-like in the surface region. These bond changes have already been shown by Appelbaum and Hamann to account for the observed surface states spectra on the Si(111) 7×7 surface, although their calculation was done for Si(111) 1×1. They inferred[7] that "very small energies and atomic displacements separate these two structures." Our ripple model with its vanishingly small perturbation amplitude is therefore consistent with the concepts advanced for this surface by Appelbaum and Hamann.

Over a temperature range of 80 °C near 800 °C the Si(111) 7×7 pattern gradually changes to a Si(111) 1×1 pattern.[6] This implies that the perturbation amplitudes γ_1 and γ_3 gradually decrease to zero in this temperature range. The temperature dependence of γ_1 and γ_3 can perhaps be accounted for by a differential thermal expansion of the rippled and undistorted portions of the lattice.

Adsorbates which preserve the Si(111) 7×7 pattern include[10] H and[11] Ga; an adsorbate which destroys the pattern at 0.04-monolayer coverage is Cl.[6] It is not clear how to unambiguously relate this adsorbate information to the proposed model.

The ripple deformation may have implications for other systems of interest. These include periodic deformations at the Si-SiO_2 interface, and large periodic deformation on the surface of certain III–V crystals such as GaAs(100) and Ge(111) which have an 8×2 structure. The periodic ripple deformation may also be the progenitor of dislocations in epitaxial growth.

The periodic surface excitation models cited from from the theoretical literature also predict ripple distortions that generate expanded periodicities in the surface plane. As mentioned in Sec. I , it is not clear at this writing whether the stress-relaxation model or the surface-relaxation models are more realistic, nor is it clear that they are unrelated. Neither approach apparently *predicts* the 7×7 periodicity from first principles, while both appear to accommodate this periodicity. Also, both models predict a surface-phase transition over a narrow temperature range (not quantitatively indicated) over which the fractional-order LEED pattern (i.e., the superlattice) should disappear. The apparent success of the contracted double layer (graphitic) approximation in reproducing the rotational symmetries of the fractional-order LEED patterns appears to argue in favor of the stress-relaxation model. However, further experimental and theoretical investigation is required to clarify the physical origin and the detailed atomic structure of this surface.

ACKNOWLEDGMENT

We wish to thank M. Bonn and G. Cisneros for help with the experiments.

*Supported by ONR Grant No. N00014-75-C-0394, Army Research Office Grant No. DAHC-04-74-60133, NSF Grant No. GK38575, and the Mobil Foundation.

[1]J. J. Lander and J. Morrison, J. Appl. Phys. 34, 1403 (1963).
[2]J. C. Phillips, Surf. Sci. 40, 459 (1973).
[3]K. C. Pandey and J. C. Phillips, Phys. Rev. Lett. 34, 1450 (1975).
[4]N. R. Hansen and D. Haneman, Surf. Sci. 2, 566 (1964).
[5]W. A. Harrison, Surf. Sci. 55, 1 (1976).
[6]J. V. Florio and W. D. Robertson, Surf. Sci. 22, 459 (1970).
[7]J. A. Appelbaum and D. R. Hamann, Phys. Rev. Lett. 31, 106 (1973).
[8]J. A. Appelbaum and D. R. Hamann, Phys. Rev. Lett. 32, 225 (1974).
[9]W. H. Zachariasen, Acta Cryst. 2, 94 (1949).
[10]H. Ibach and J. E. Rowe, Surf. Sci. 43, 481 (1974).
[11]G. Margaritondo, S. B. Christian, and J. E. Rowe, J. Vac. Sci. Technol. 13, 329 (1976).
[12]T. E. Feuchtwang, Phys. Rev. 155, 715 (1967).
[13]S. E. Trullinger and S. L. Cunningham, Phys. Rev. Lett. 30, 913 (1973); Phys. Rev. B 8, 2622 (1973).
[14]E. Tosatti and P. W. Anderson, Solid State Commun. 14, 773 (1974).
[15]J. D. Levine, P. Mark, and S. H. McFarlane, J. Vac. Sci. Technol. 14, 878 (1977).
[16]J. D. Levine, P. Mark, and S. H. McFarlane, Phys. Rev. Lett. 38, 1408 (1977).
[17]C. W. Tucker and C. B. Duke, Surf. Sci. 23, 411 (1970); J. Vac. Sci. Technol. 8, 5 (1971).
[18]A. F. Wells, *Structural Inorganic Chemistry* (Clarendon, Oxford, 1962), p. 770.

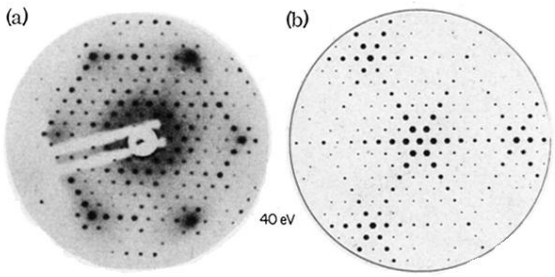

FIG. 11. Typical very low voltage (40 V) LEED patterns, showing nearly 6-fold symmetry and voltage dependence in the experimental pattern (a) but not in the theoretical pattern (b). Because the electron mean-free path is very small, only one graphitelike layer primarily contributes to the scattering.

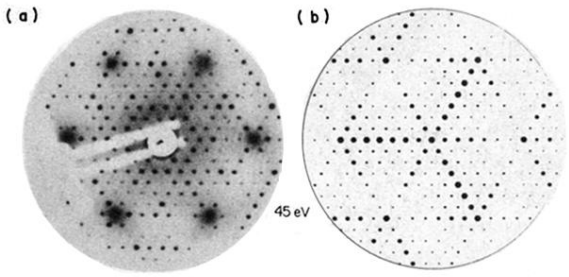

FIG. 12. Same as in Fig. 11, with $V = 45$ V.

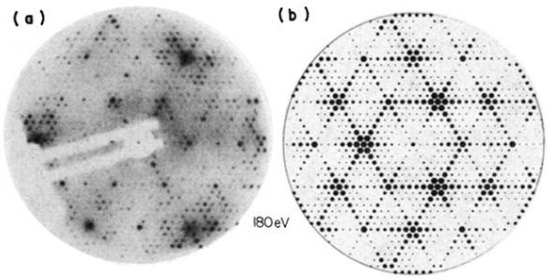

FIG. 13. Typical very-high-voltage LEED pattern. Notice the disk of low-spot intensity. Because the mean free path is large, perhaps three graphitelike layers contribute to the scattering pattern, which cannot be accounted for with only two graphitelike layers in the model. $V = 180$ V. (a) experimental. (b) theoretical.

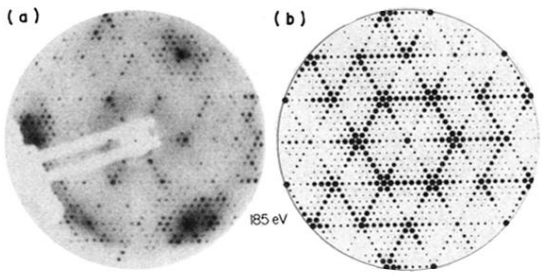

FIG. 14. Same as in Fig. 12, except $V = 185$ V.

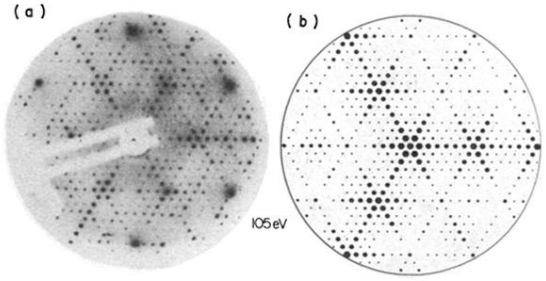

FIG. 5. "Thin propeller" LEED pattern at 105 V; (a) experimental, (b) theoretical.

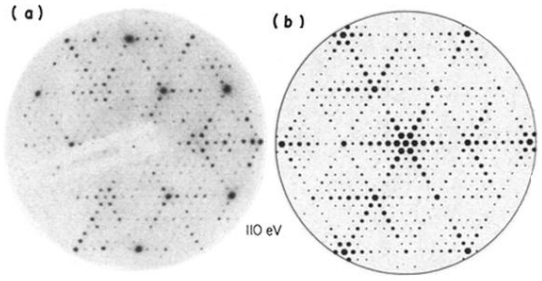

FIG. 6. "Star" LEED pattern at 110 V; (a) experimental, (b) theoretical.

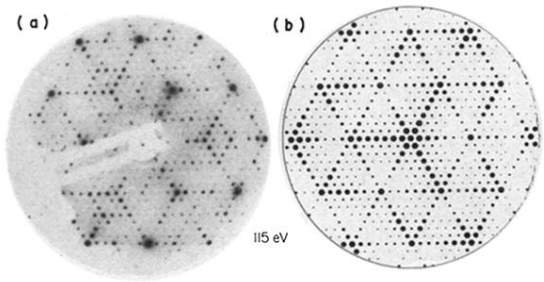

FIG. 7. Modified "star" LEED pattern at 115 V; (a) experimental, (b) theoretical.

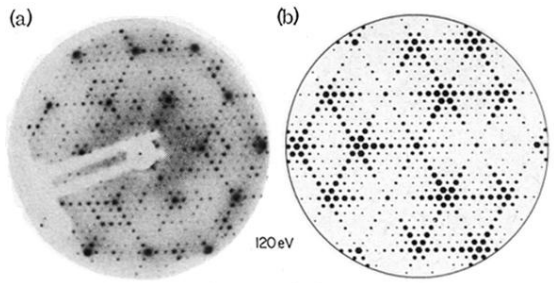

FIG. 8. "Ballantine three ring" LEED pattern at 120 V. (a) experimental. (b) theoretical.

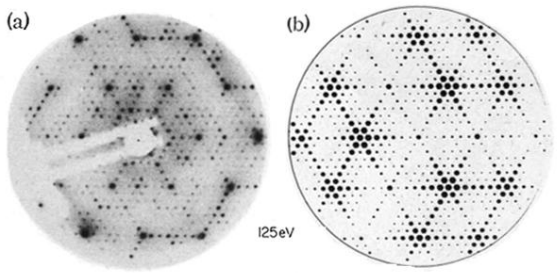

FIG. 9. Modified "Ballantine three ring" LEED pattern at 125 V. (a) experimental. (b) theoretical.